Coupling of Metals and Biominerals: Characterizing the Interface between Ferromagnetic Shape-Memory Alloys and Hydroxyapatite

Uta Allenstein,[†,‡] Susanne Selle,[¶] Meike Tadsen,[†] Christian Patzig,[¶] Thomas Höche,[¶] Mareike Zink,[‡] and Stefan G. Mayr*[†,‖,⊥]

[†]Leibniz-Institute for Surface Modification (IOM), Permoserstrasse 15, 04318 Leipzig, Germany

[‡]Soft Matter Physics Division, Faculty of Physics and Earth Sciences, University of Leipzig, Linnéstrasse 5, 04103 Leipzig, Germany

[¶]Fraunhofer Institute for Mechanics of Materials (IWM), Walter-Hülse-Strasse 1, 06120 Halle, Germany

[‖]Translational Center for Regenerative Medicine, University of Leipzig, Philipp-Rosenthal-Strasse 55, 04103 Leipzig, Germany

[⊥]Faculty of Physics and Earth Sciences, University of Leipzig, Linnéstrasse 5, 04103 Leipzig, Germany

S Supporting Information

ABSTRACT: Durable, mechanically robust osseointegration of metal implants poses one of the largest challenges in contemporary orthopedics. The application of biomimetic hydroxyapatite (HAp) coatings as mediators for enhanced mechanical coupling to natural bone constitutes a promising approach. Motivated by recent advances in the field of smart metals that might open the venue for alternate therapeutic concepts, we explore their mechanical coupling to sputter-deposited HAp layers in a combined experimental–theoretical study. While experimental delamination tests and comprehensive structural characterization, including high-resolution transmission electron microscopy, are utilized to establish structure–property relationships, density functional theory based total energy calculations unravel the underlying physics and chemistry of bonding and confirm the experimental findings. Experiments and modeling indicate that sputter-deposited HAp coatings are strongly adherent to the exemplary ferromagnetic shape-memory alloys, Ni−Mn−Ga and Fe−Pd, with delamination stresses and interface bonding strength exceeding the physiological scales by orders of magnitude.

KEYWORDS: hydroxyapatite, smart metals, HR-TEM, DFT, adhesion
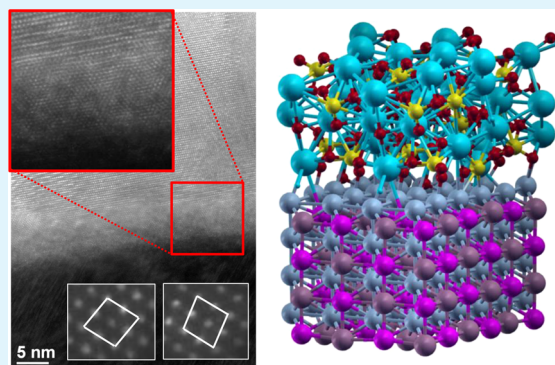
1. INTRODUCTION

Ferromagnetic shape-memory alloys, such as the Ni_2MnGa[1] and Fe_7Pd_3[2] systems, have attracted considerable interest as contemporary smart materials that can yield magnetically inducible strains as large as several percent,[3] as well as magnetization changes upon straining.[4] Besides the ferromagnetic shape-memory effect, these alloys also reveal all features of "traditional" thermal shape-memory alloys and thus can be regarded as a Nitinol (NiTi)[5] substitute, additionally extending its capabilities toward magnetic actuation. They are thus, from a conceptual point of view, ideally suited as variable mechanical transducers for use in hazardous and biomedical environments, where the temperature has to be kept constant. With the goal of application of these alloys as active elements in vivo, establishing a pertinent mechanical link to cells, tissues, and bones constitutes one of the largest challenges. In terms of coupling to cells and tissues, previous studies[6,7] have demonstrated highly favorable properties of Fe_7Pd_3, which promises reliable in vivo use, particularly when appropriately functionalized.[8] For attaching ferromagnetic shape-memory implants to bones, e.g., by employing their ferromagnetic shape-memory behavior for rigid attachment into the femoral canal of a bone, requirements are different in the sense that (i) coupling between the bone and implant has to be able to withstand much higher forces without loosening and (ii) precautions regarding cytotoxic components can practically be less strict because implants are frequently embedded inside the bone and treated by appropriate surface finishing prior to that, which might be particularly relevant in the case of Ni−Mn−Ga. Clearly, the establishment of a sufficiently strong and durable mechanical link between the bone and implant is highly desirable, which will be in the center of focus of the current paper. With the goal of optimum bone−implant interaction, we presently explore the capabilities of bone−mimetic hydroxyapatite (HAp) coatings to mediate the mechanical coupling between the bone and implant. In doing so, the bonding strength between HAp and Ni_2MnGa as well as Fe_7Pd_3 ferromagnetic shape-memory alloys will be considered in depth. Focusing on this interface is motivated by the fact that the strength of the second interface, viz., between bone−

mimetic HAp and natural bone, is already well-established at this point.[9]

Hydroxyapatite $Ca_{10}(PO_4)_6(OH)_2$ is a calcium phosphate bioceramic that is very similar to the primary mineral constituent of human bone tissue, dental enamel, and dentin. Because of the material's excellent bioactivity, biocompatibility, and mechanical properties, HAp coatings are already widely used for orthopedic and dental implants. The enhanced osteoconductivity can provide a faster implant fixation and bone remodeling and promote the biological performance.[10] In a biological environment, crystalline HAp exhibits the lowest solubility of all common calcium phosphates,[11] which renders this material a prime candidate to realize a robust adhesive coating on Ni−Mn−Ga and Fe−Pd. Several HAp coating strategies have been investigated and are still the subject of current research, including plasma spraying, sol−gel, pulsed-laser deposition, electrophoresis deposition, dip-coating, ion-beam methods, and sputtering. An overview of the different techniques can be found in ref 12. To date, thermal plasma spraying is the most widely used method to fabricate HAp coatings and the only one employed commercially. However, plasma-sprayed coatings suffer from a number of issues, including poor adhesion to a metallic substrate, nonuniform density, high porosity, and a high fraction of amorphous calcium phosphate. Radio-frequency (RF) magnetron sputtering is a relatively new HAp deposition technique and shows some advantages over conventional plasma spraying. Previous studies primarily on HAp coatings of conventional Ti/Ti−alloy implant materials indicate that large substrate areas can be coated with homogeneous and well-adherent HAp films.[13]

With this background, the present work explores the structural properties and adhesion strength of HAp coatings on Ni−Mn−Ga as well as Fe−Pd ferromagnetic shape-memory alloys, employing experiments on sputter-deposited thin films as well as density functional theory (DFT) ab initio computer modeling.

2. MATERIALS AND METHODS

2.1. Synthesis of Ni−Mn−Ga and Fe−Pd Ferromagnetic Shape-Memory Alloy Thin Films. Ni_2MnGa thin-film samples used in this study are prepared by direct-current (dc) magnetron sputtering from a $Ni_{49}Mn_{32}Ga_{19}$ target. The vacuum achieved a base pressure of 10^{-6} mbar or better after bake-out. The substrate−target distance was set to 9 cm for both deposition processes. At an argon process pressure of 3×10^{-3} mbar, the Ni−Mn−Ga films were deposited on $(10 \times 10 \times 0.5)$ mm^3 (001)-oriented MgO single crystals. Using a dc power of 50 W, 400-nm-thick films were prepared at a deposition rate of 0.19 nm/s. The substrate temperature was kept at 600 °C during sputter deposition, which proved to be the optimum conditions in terms of structural homogeneity as well as film smoothness and integrity. While lower temperatures resulted in rough inhomogeneous surfaces, films prepared at higher temperatures reveal manganese loss [see the Supporting Information (SI), Figure S1, for details]. After deposition, the heating power is reduced rapidly to limit manganese loss due to evaporation. Fe_7Pd_3 ferromagnetic shape-memory alloy thin films, on the other hand, were grown in ultrahigh-vacuum conditions (base pressure of 10^{-9} mbar or better) on MgO (001) single crystals at substrate temperatures as high as 900 °C by molecular beam epitaxy. As described previously in detail,[14] they were subsequently quenched at sufficiently high cooling rate to obtain the desired face-centered tetragonal (fct) martensite phase, which is a prerequisite for magnetic actuation. As demonstrated previously, both Ni−Mn−Ga and Fe−Pd films fulfill all requirements in terms of the thermodynamic phase necessary for magnetic actuation, viz., the 14 M modulated and fct martensite phases, respectively.[15,16]

2.2. HAp Coatings. Subsequent to characterization of the metal films, a HAp coating of approximately 700 nm is sputtered on top of them using 13.56 MHz RF plasma excitation. To prevent the HAp target (sintered crystalline HAp powder) from cracking,[17] we use a low power of 25 W at 10^{-3} mbar of argon pressure, resulting in a long deposition time of 70 h.

2.3. Sample Characterization. Ni−Mn−Ga and Fe−Pd samples were investigated regarding their surface topography by scanning electron microscopy (SEM) and atomic force microscopy (AFM) using a Zeiss "Ultra 55" (In-lens SE detector; electron acceleration voltage, 5 kV) and Asylum Research "MFP-3D SA AFM10", respectively. Chemical compositions of the samples were determined by energy-dispersive X-ray spectrometry (EDX) with a Bruker AXS "XFlash Detector 3001" at an electron acceleration voltage of 15 kV. To allow for a higher accuracy and to suppress quantization errors due to the signal from the MgO substrate, samples with an increased film thickness (Ni−Mn−Ga/Fe−Pd films, 1.0 μm; HAp, 1.4 μm) were used. Because small composition variations (within detection limits) result in a relatively severe modification of martensite−austenite transition temperatures, these temperatures were determined individually by differential scanning calorimetry (DSC) and resistivity measurements, when required. The compositional homogeneity was verified by secondary-ion mass spectrometry (SIMS) with an IONTOF "TOF.SIMS 5". Because of the complex crystal structure of epitaxial martensitic Ni−Mn−Ga thin films, simple $\theta - 2\theta$ X-ray diffraction (XRD) measurements are not sufficient to characterize the samples, and more elaborate pole figure measurements were carried out with a Seifert "XRD 3003 PTS" four-circle diffractometer using Cu Kα radiation. The calcium phosphate coatings were investigated by attenuated total reflectance Fourier transform spectroscopy (ATR-FTIR) with a Bruker "BIFS55" spectrometer. Finally, the interface between the coating and metal film was imaged by high-resolution transmission electron microscopy (HR-TEM) with both an FEI "Tecnai" and an FEI "TITAN^3 G2 80-300" microscope, extending previous studies on Ni−Mn−Ga thin films.[15]

2.4. Delamination Tests. To characterize the coating adhesion strength, a "Inspekt Mini 3kN" tensile testing machine obtained from Hegewald & Peschke was employed to disjoin the HAp coatings from the Ni−Mn−Ga and Fe−Pd substrates. This machine was modified to load two steel stamps between which the Ni−Mn−Ga and Fe−Pd samples were glued with "Torr Seal" (a sealant resin glue for vacuum applications from Agilent Technologies) and 3 M Scotch Weld DP 810 (dried for 10 min at 65 °C, as recommended), respectively. Glue on the coating-side stamp was removed along the sample edges to prevent errors caused by adhesion to the MgO substrate. The bottom stamp was fixed to the machine, and the coating-side top stamp was grabbed by a claw and the force transducer. The transducer moved 0.5 mm/min and recorded the force required to pull the pieces apart. From the resulting force−displacement curves, the maximum force and work of delamination were determined.

2.5. Ab Initio Calculations. To theoretically predict the adhesion strength and unravel the physics and chemistry of bonding between HAp and ferromagnetic shape-memory alloys Ni_2MnGa and Fe_7Pd_3, respectively, we conducted DFT-based total energy calculations, as implemented in the *PWSCF* code.[18] Ultrasoft pseudopotentials based on the atomic reference configurations [Ar] $3d^9 4s^1$, [Ne] $3s^2 3p^6 3d^5 4s^2$, [Ar] $3d^{10} 4s^2 4p^1$, [Ar] $3d^7 4s^1$, [Kr] $4d^9 5s^1$, [Ne] $3s^2 3p^6 4s^2$, [Ne] $3s^2 3p^3$, [He] $2s^2 2p^4$, and $1s^1$ for Ni, Mn, Ga, Fe, Pd, Ca, P, O, and H, respectively, were utilized[19] in combination with a plane-wave basis set (energy cutoff, 476.2 eV; augmentation charges, 4762 eV). All of the pseudopotentials had been thoroughly tested prior to use; in particular, they showed excellent agreement with independent predictions based on the projected augmented wave approach.[20,21] State-of-the-art DFT calculations still allow for only a very limited number of atoms, which constitutes a particular challenge for the disordered Fe_7Pd_3 alloy, which we presently treat with a special quasirandom structure approach that was already successfully employed previously.[21] After preparation of the simulation cells, the latter are subsequently relaxed under appropriate boundary conditions, using a Broyden−Fletcher−Goldfarb−Shanno scheme (accuracy

threshold of 0.03 meV or better). Careful convergence studies were performed with respect to the Monkhorst−Pack-type[22] k-point mesh, which was chosen to be denser than 2.5 irreducible k points per atom, in combination with Methfessel−Paxton smearing[23] (0.2 eV). On the basis of fully relaxed configurations, the binding and surface energies were determined, while the chemistry of bonding was assessed using the density of states, densities of states projected onto individual atomic orbitals, and charge distributions due to Bader analysis.[24] The results were visualized in *XCrysDen*.[25]

3. EXPERIMENTAL RESULTS AND DISCUSSION

3.1. Overview of Ferromagnetic Shape-Memory Films. The compositions of both sputter-deposited Ni_2MnGa and vapor-condensed Fe_7Pd_3 films were routinely verified with EDX for all samples synthesized. While the deposition conditions for Fe_7Pd_3 were chosen to reveal the exact stoichiometries, sputter deposition from the Ni_2MnGa target results in an average film composition of $Ni_{49\pm2}Mn_{31\pm1}Ga_{20\pm1}$ (atomic percent). For both material systems, SIMS measurements indicated an absence of composition gradients along the film thickness. Martensite−austenite transition temperatures were tracked down by resistivity and DSC measurements, yielding 328 ± 10 and 318 ± 13 K for Ni−Mn−Ga and Fe−Pd, respectively, with the martensite start and finish temperatures located at the lower and upper boundaries of the interval, respectively. An exemplary DSC measurement on Ni−Mn−Ga is shown in the SI, Figure S2. XRD measurements identify the presence of an orthorhombic 14 M crystal structure at room/body temperature (Figure 1), with a and c axes tilted at 3° with
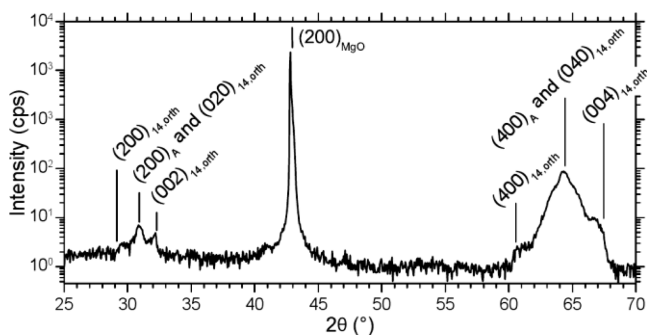

Figure 1. $\theta/2\theta$ diffractogram of a martensitic 1-μm-thick film. The sample tilt and rotation had been adjusted to receive intensities for all three $\{100\}_{14M}$ lattice planes according to the orthorhombic crystal structure. It is interesting to note that the calculated powder diffractogram, using the program *PowderCell*,[26] predicts an extinction (destructive interference) of the three $\{200\}_{14M,orth}$ reflections. However, these calculations assume a perfect single crystal, and small deviations from the given structure (e.g., substitutional atoms) can partially eliminate the extinction.

respect to the surface normal for martensitic Ni−Mn−Ga thin films; the relevant pole figures in stereographic projections can be found in Figure 2.

Fe−Pd, on the other hand, resides in the fct martensite phase at these temperatures, as was already demonstrated in detail previously.[16]

3.2. HAp Coatings. The deposited HAp coatings, on Ni−Mn−Ga and Fe−Pd as well as on plain MgO substrates, exhibit a smooth and featureless surface with an root-mean-square roughness of 3 nm. EDX determined a Ca/P ratio of 1.70 ± 0.5 (see the SI, Figure S3), which closely resembles that of "ideal" HAp (1.66). By ATR-FTIR, most of the characteristic

phosphate PO_4^{3-} vibration absorption peaks of HAp are recovered (see Figure 3 and Table 1). However, deviating absorption intensities with respect to the target material and the absence of the hydroxyl stretch peak were observed. The spectrum exhibits carbonate CO_3^{2-} absorptions, which were also present in the target. No diffraction peaks originating from the coating were observed in XRD measurements.

3.3. HR-TEM Structural Characterization of the Ni−Mn−Ga/HAp System. The Ni−Mn−Ga/HAp double layer prepared on MgO substrates is selected for exemplary in-depth analysis using HR-TEM characterization. To do so, TEM lamellae are prepared from the *as-prepared* sample using a focused-ion-beam system (Carl Zeiss Auriga Laser FIB workstation) and subsequently argon-ion-beam-thinned (using a Fischione NanoMill). First the structure of the Ni−Mn−Ga films is addressed, which is dominated by twin variants of 14 M martensite (Figure 4). Nanodiffraction unveils the presence of an orthorhombic bc unit cell oriented in the [010] direction. The tilt angle between different martensite variants is determined as $96 \pm 1°$, which agrees with the theoretical value of 96° expected for 14 M martensite[28] and results in the structural model sketched in Figure 4. The film grows epitaxial (cube-on-cube) on the MgO substrate. As determined in Figure 4, the epitaxial relationship is given by Ni−Mn−Ga(001) [110]‖MgO(001)[100]; i.e., the Ni−Mn−Ga unit cell is aligned along the diagonal of the MgO unit cell, as observed before.[15] The morphology of the Ni−Mn−Ga/HAp interface, on the other hand, is dominated by a twin-related surface relief, as characterized also by AFM previously.[20] An EDX scan performed across the lamella within HR-TEM does not yield any signs of compositional heterogeneity within Ni−Mn−Ga or interdiffusion with MgO or the HAp constituents (see the SI, Figure S4).

The HAp coating, on the other hand, is characterized by a polycrystalline microstructure, as confirmed by a HR-TEM cross section and selected-area diffraction (SAD; see the SI, Figure S5). Most lattice planes in the coating can be indexed according to the HAp crystal structure. However, the small grain size prevents a precise determination of the lattice plane distances, and also other calcium phosphate phases could be present. The transition between Ni−Mn−Ga and HAp proceeds relatively fast with no signs of intermixing, despite a slight calcium and oxygen penetration into the Ni−Mn−Ga surface, as determined by EDX mapping (Figure 5). As for the orientation relationship between Ni−Mn−Ga and HAp, SAD unveils that twin variants and HAp polycrystals are well aligned (see the SI, Figure S6).

3.4. Mechanical Strength of the Ni−Mn−Ga/HAp and Fe−Pd/HAp Interfaces. The delamination test of a 4.0×4.8 mm^2 HAp-coated Ni−Mn−Ga sample is shown in Figure 6. Because the head piece is gripped by three screws at slightly different positions, an irregular pattern related to straining of the latter is observed prior to the actual pull-off process. Delamination occurs in the course of the final decay of the displacement−force curve, which is also employed to quantify the related work by numerical integration. After separation, the force transducer registers the weight of the top stamp that is corrected for during data analysis. Except for a still-coated, circular area of 100 nm diameter, SEM micrographs verified a clean delamination of the coating. No trace of calcium or phosphorus could be detected by EDX on the metal side. The work required to separate Ni−Mn−Ga and HAp coating (work of delamination) was determined as 1.6 J/m^2. The transducer
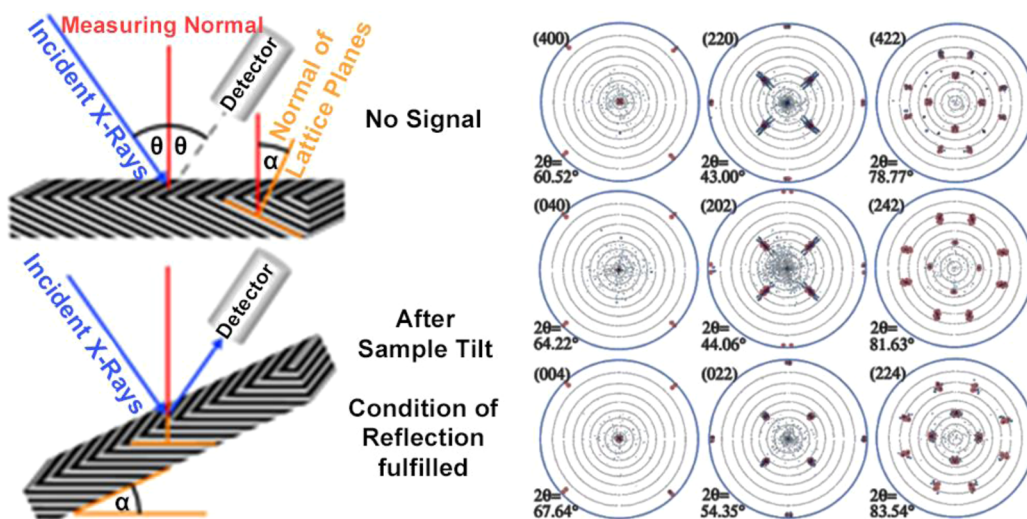
Figure 2. Pole figures for 1-μm-thick Ni−Mn−Ga films: signal interpretation and contour plots. The recorded data (sample rotation ϕ, tilt angle α, and intensity) contain the distribution of the present lattice plane orientations and can be visualized using a stereographic projection. By movement from the center to the outermost circle, α increases from 0° to 90°. A scale bar has been omitted because the intensity of a recorded peak does not necessarily correspond to the maximum value because of the finite step size. Cells with the $a_{14M,orth}$ and $c_{14M,orth}$ axes tilted approximately 3° from the surface normal are prevalent. The diffraction spot in the center of the (040) orientation can originate from untilted austenite or 14 M cells with the $b_{14M,orth}$ axis perpendicular to the surface. Pole figure modeling using the "CaRIne Crystallography" software[27] using 18 differently oriented 14 M orthorhombic unit cells yields reasonable agreement. These include a unit cell with $a_{14M,orth}$ perpendicular to the film surface and $b_{14M,orth}$ parallel to [100] MgO tilted 3° around its $b_{14M,orth}$ axis. Afterward, this cell is additionally rotated and copied to 45°, 135°, 225°, and 315° positions around the surface normal. The $b_{14M,orth}$ axis is now parallel to [110] MgO. This procedure is repeated for a tilt around $c_{14M,orth}$ and additionally for cells with $c_{14M,orth}$ perpendicular to the surface, yielding in total 16 orientations. Finally, two untitled unit cells with $b_{14M,orth}$ perpendicular to the surface, with rotations of 45° and 135°, are added. Further refinement would possibly require more elaborate techniques and the accounting of the full 14 M modulation.
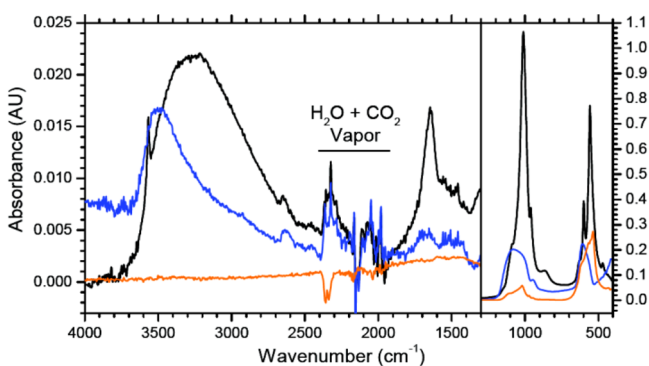

Figure 3. Characterization of the calcium phosphate coating on Ni−Mn−Ga thin films. ATR-FTIR absorbance spectrum of HAp powder (black), a HAp layer on Ni−Mn−Ga (blue), and a HAp layer on heated MgO (orange). AU denotes absorbance units.

Table 1. Absorption Peak Positions of Figure 3 $(cm^{-1})^a$

peak type	HAp powder	compound	heated MgO
hydroxyl stretch	3568		
carbonate	1649	≈1680	
	1458	≈1470	
	1419		
phosphate ν_3	1088	≈1087	1099
	1011	≈1030	1016
phosphate ν_1	960	950	
phosphate ν_4	625	≈622	620
	600	≈600	580
	558		558
phosphate ν_2	473		

$^a\nu_i$ denotes the different vibrational modes of the PO_4^{3-} functional groups.

registered a peak stress/adhesion strength of 0.25 MPa during measurement. In comparison to that, adhesion of HAp to Fe−Pd was measured (see the SI, Figure S7). None of the measured samples failed at the interface of HAp and Fe−Pd. Instead, failure within the HAp layer was observed at peak stresses of 3.2 N/mm². This indicates that not the interface but HAp itself constitutes the mechanically weak link. The related work of HAp rupture is determined as 4.65 J/m².

4. AB INITIO TOTAL ENERGY CALCULATIONS AND DISCUSSION

4.1. Ni−Mn−Ga. With the aim of clarifying the physics of bonding between Ni−Mn−Ga and HAp, DFT-based total energy calculations are conducted using the techniques described in the Materials and Methods section. Starting

from the "literature data" for crystalline HAp, we first performed structural relaxation runs toward the overall ground state of a perfect infinitely extended HAp crystal at zero stress in its orthorhombic 88-atom supercell. The obtained lattice parameters of $a = 0.955$ nm and $c = 0.690$ nm of the hexagonal unit cell are in excellent agreement with experiments ($a = 0.942$ nm and $c = 0.688$ nm, respectively).[29] Similarly, six non-modulated martensitic Ni₂MnGa unit cells (tetragonal) are attached along their a axes to yield a $1 \times 3 \times 2$ supercell, which is subsequently stretched along the x and y directions to match the corresponding dimensions of the HAp unit cell. The latter is subsequently structurally relaxed, imposing a fixed cell size along the x and y directions, as well as zero pressure along the z axis. By insertion of a sufficiently large "vacuum" layer in the z direction and structural relaxation of the resulting supercells at fixed cell sizes, the surface energies along the (001) planes of
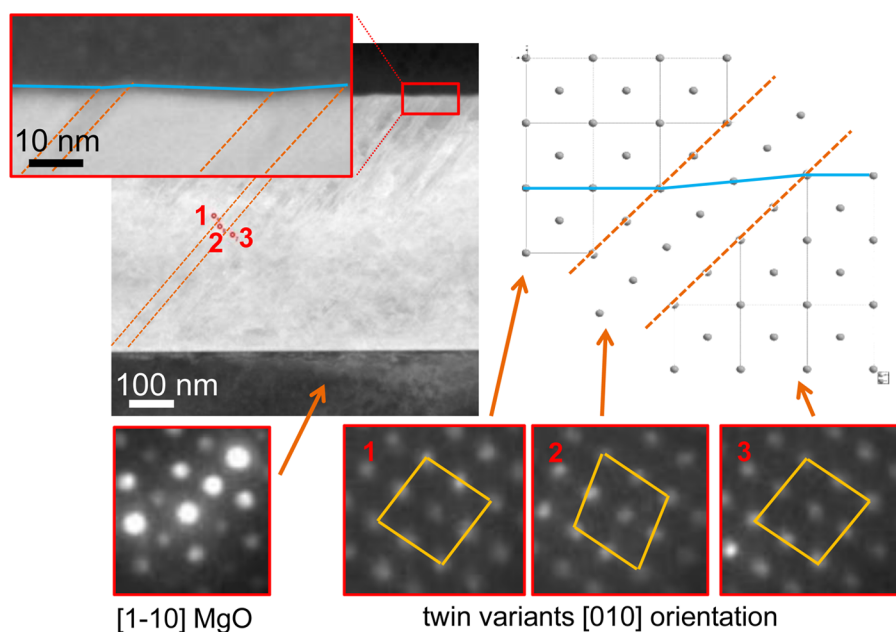
Figure 4. TEM micrographs of the sample cross section. In the overview image, twin boundaries at an angle of 45° with respect to the sample surface can be seen in the metal film (dashed lines). Nanodiffraction unveils orthorhombic Ni−Mn−Ga unit cell variants with [010] orientation; the twin variants are aligned with an angle of 96 ± 1°, as expected for 14 M martensite. The MgO/Ni−Mn−Ga interface is characterized by a Ni−Mn−Ga(001)[110]∥MgO(001)[100] epitaxial relationship, while the Ni−Mn−Ga/HAp interface is morphologically dominated by twin variants.
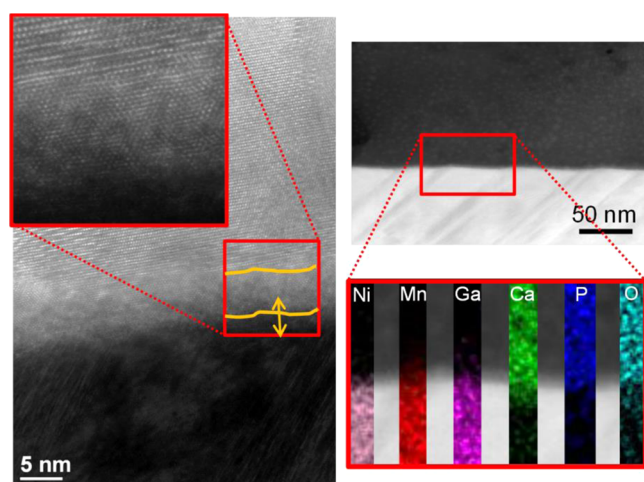
Figure 5. HR-TEM and EDX measurements across the transition region between Ni−Mn−Ga and HAp. Transition proceeds structurally and compositionally within a thickness of 5−6 nm.

the supercells are calculated, yielding 1.65 and 1.93 J/m^2 for HAp and Ni−Mn−Ga, respectively. The application of nonmodulated instead of 14 M martensite within these supercells is motivated by its own technical relevance and the lower computational costs that make the problem treatable with current resources, while the chemistry of bonding turns out to be governed by the elemental constituents and thus is expected to reveal no fundamental differences.

The former value can, in fact, be compared to half of the experimental rupture work, 4.65/2 = 2.32 J/m^2, determined in the course of the delamination test performed on the Fe−Pd/HAp system. Clearly, the main source of discrepancy to the experiments is their irreversible nature, viz., the presence of energy dissipation. These surfaces are subsequently joined together, yielding the layered Ni−Mn−Ga/HAp supercell

shown in Figure 7. When extensive structural relaxation is performed under fixed x and y dimensionalities and zero stress in the z direction, the interface energy between HAp and Ni−Mn−Ga is determined as 2.39 J/m^2, taking the infinite crystals as the reference state. To quantify the cohesion between HAp and Ni−Mn−Ga, the cohesive energy of the interface is of particular relevance, which we define as the energy required to disjoin HAp from Ni−Mn−Ga by creating open surfaces. It is readily determined as 2.39 J/m^2 − (1.65 J/m^2 + 1.93 J/m^2) = −1.19 J/m^2. Because it describes the reversible work required to open the interface in the zero temperature limit, it constitutes a suitable measure for comparison with experiments. The latter, in fact, reveal a slightly higher value of 1.6 J/m^2, the largest contribution to deviation presumably resulting from violating the reversibility, viz., the presence of dissipative contributions in experiments. As for the bonding conditions at the Ni−Mn−Ga/HAp interface, atomic configurations displayed in Figure 7 already give a first hint that interaction for the present configuration might be mediated primarily by Ca−Ni, P−Ni, and O−Ni bonds. The presence of chemical bonds is, in fact, corroborated by contemplating the densities of states projected onto atomic orbitals of the potential bonding partners. As expected, it unveils energetic overlaps of the O and P p$_z$ as well as, to a somewhat minor extent, p$_x$ and p$_y$ orbitals with the Ni−Mn−Ga d band, whereas resonances between d states and the Ni−Mn−Ga d band dominate in the case of calcium. The presence of charge transfer between HAp and Ni−Mn−Ga is explored by performing Bader analysis on infinite, periodic HAp cells and the supercell of Figure 7, viz., before and after binding HAp to Ni−Mn−Ga. This indicates the transfer of one electron from Ni−Mn−Ga to HAp per hexagonal unit cell or, equivalently, an average of 0.02 electrons per HAp atom. From these considerations, it becomes clear that the overall charge transfer only constitutes a minor effect in Ni−Mn−Ga/HAp bonding. However, Bader analysis yields a highly relevant role of charge shifts in bonding of [PO$_4$]$^{3-}$
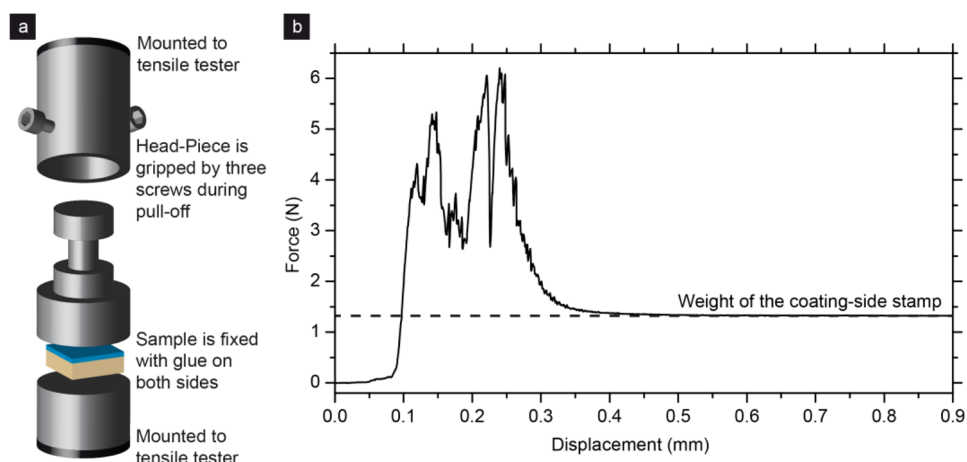
Figure 6. Delamination test: (a) Sketch of the self-constructed sample mounting stage. (b) Force−displacement diagram of the pull-off measurement. An irregular pattern during measurement is produced by the slightly delayed gripping of the claw.
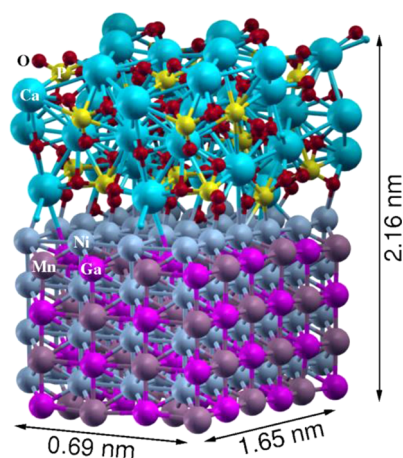

Figure 7. Relaxed supercell consisting of layers of nonmodulated martensitic Ni_2MnGa and attached crystalline HAp ($Ca_5[OH|(PO_4)_3]$), comprised of 96 and 88 atoms, respectively. Because of the adaptive nature of martensite, the dimensions within the interface plane were set to equilibrium values of an infinite HAp single crystal. Bonds shown here are based on a simple connectivity criterion (the distance is less than the sum of covalent radii × 1.05).[30]

groups to Ni−Mn−Ga. It occurs by (i) a shift of an unbound electron pair from O toward Ni−Mn−Ga (in the sense of a coordinate bond) and (ii) a shift of electrons from Ni−Mn−Ga toward P, raising its coordination number to 5. In addition to establishment of the chemical types of bonds, both effects (i) and (ii) prove to be highly efficient in shielding the multipole character of $[PO_4]^{3-}$ by mobile charges in Ni−Mn−Ga d bands, additionally reducing the energy.

4.2. Fe−Pd. Looking at the total energy of the Fe−Pd/HAp system in comparison to the bulk of each subsystem reveals that it is energetically profitable to form an interface of the two materials. The upper part of Figure 8 illustrates an energy profit at the interface of 0.85 J/m². Compared to the individual bulks, the Ewald contribution, related to ion−ion interactions, decreases by 8%, while one-electron contributions increase by 15%.

To understand bonding at the Fe−Pd/HAp interface more deeply, further postprocessing was necessary. The total density of states depicted in Figure 8 shows that the distribution for the Fe−Pd/HAp system combines from the bandlike configuration

of the Fe−Pd bulk and the molecular-orbital-like configuration of HAp. This can be evaluated more clearly when looking at the projected density of states of each atom. Those reveal that particularly iron atoms at the interface show a nonzero density of states at energies between 5.4 and 6.7 eV that can be attributed to the p orbitals of oxygen atoms from HAp. Figure 8 illustrates this overlap, by displaying an isosurface of the integrated local density of states at the interface. The green circles mark the spots of nonzero electron density between oxygen and iron atoms, while within the bulk of the HAp, a nonextended shape of the oxygen p orbitals can be seen.

Bader charge analysis confirms the importance of the Fe−O bond to the interface. Charge transfer is visible between palladium and calcium, palladium, and phosphorus, where palladium atoms gain on average 0.08 electrons/bond. However, in comparison, the gain of 0.25 electrons/bond for the oxygen atom in the Fe−O bond is much higher.

Therefore, we performed force−distance calculations on the Fe−O bond and calculated a peak force of 7.74 nN and a charge transfer of 0.83 electrons between the two respective atoms. This force is reached at a distance of 2 Å, which is also the average distance for iron and oxygen atoms at the Fe−Pd/HAp interface. Here, energy contributions suggest a dominance of coulomb interactions. Thus, one can assume the force to be proportional to the charge of the participating atoms. When other influences are ignored, this assumption leads to a peak force of 0.41 nN for an Fe−O bond at the Fe−Pd/HAp interface. With an average of five such bonds per interface of the simulated cell, this leads to a peak force per surface area of 1.8 GPa.

5. CONCLUSIONS

Employing experiments and ab initio calculations, we have explored structural and mechanical coupling of the two most prominent representatives of the upcoming materials class of ferromagnetic shape-memory alloys, Ni−Mn−Ga and Fe−Pd, in their magnetically active 14M and fct phases, respectively, to sputter-deposited HAp coatings. For the Ni−Mn−Ga/HAp system, an in-depth HR-TEM analysis unveils a polycrystalline nature of the HAp coating, with a strong orientation relationship to the metal underneath. Mechanically, this is reflected by a decent strength of the Ni−Mn−Ga/HAp interface with a theoretical bonding energy of −1.19 J/m² (DFT) as well as an experimental work of delamination of 1.6
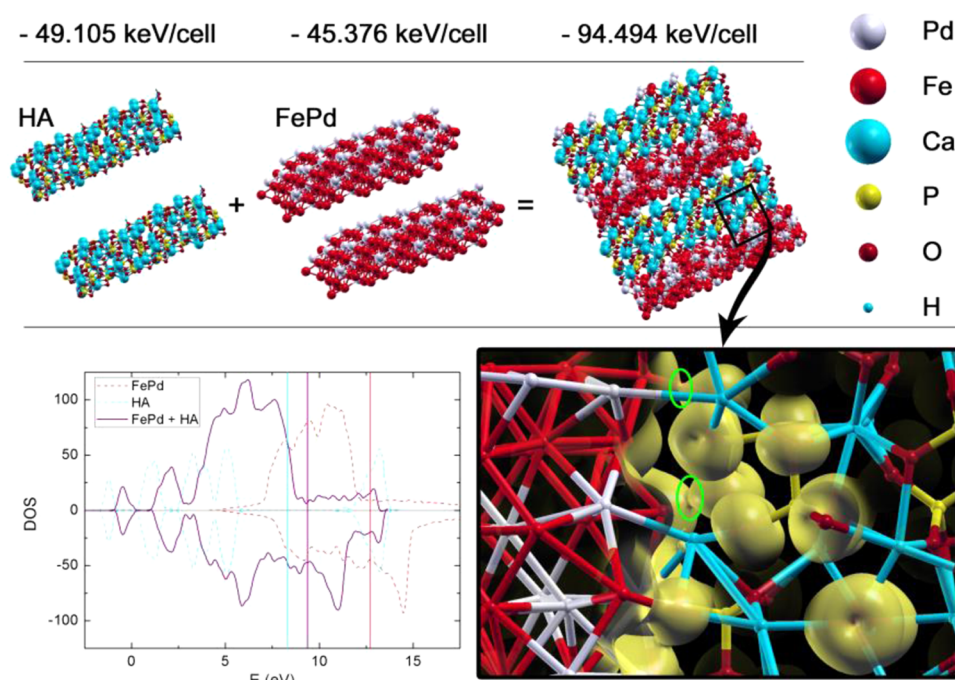
Figure 8. Upper part: energy profit from interfacing HAp and Fe—Pd bulks to a merged Fe—Pd/HAp system. Lower part: total density of states of the bulk compared to the merged system. The display of an isosurface at around 6.1 eV illustrates the overlap of oxygen orbitals within HAp with bands from Fe—Pd (green circles).

J/m^2 and a rupture stress of 0.25 MPa. For the Fe—Pd/HAp interface, experiments indicate a mechanical strength exceeding that of pure HAp. This is confirmed by DFT calculations, which predict a binding energy of 0.85 J/m^2 and a rupture force as large as 1.8 GPa. Chemically, in both cases this interaction is mediated by strong interactions of electrons around calcium, phosphorus, and oxygen with the d bands of the metals. In both cases, the mechanical strengths of the interfaces certainly exceed typical stresses relevant under physiological conditions. The proposed coating strategy and understanding from the experimental—theoretical studies within the present article might thus prove useful for advanced osseointegration concepts in medical therapy and beyond.

ASSOCIATED CONTENT

Ⓢ Supporting Information

SEM micrographs, DSC measurements, EDX spectra, SAD diffraction patterns, and force—displacement curves from delamination tests. The Supporting Information is available free of charge on the ACS Publications website at DOI: 10.1021/acsami.5b03189.

AUTHOR INFORMATION

Corresponding Author
*E-mail: smayr@uni-leipzig.de.

Notes
The authors declare no competing financial interest.

ACKNOWLEDGMENTS

REFERENCES

(1) Ullakko, K. Magnetically Controlled Shape Memory Alloys: A New Class of Actuator Materials. *J. Mater. Eng. Perform.* **1996**, *5*, 405–409.

(2) Cui, J.; Shield, T.; James, R. Phase Transformation and Magnetic Anisotropy of an Iron-Palladium Ferromagnetic Shape-Memory Alloy. *Acta Mater.* **2004**, *52*, 35–47.

(3) Sozinov, A.; Likhachev, A.; Lanska, N.; Ullakko, K. Giant Magnetic-Field-Induced Strain in NiMnGa Seven-Layered Martensitic Phase. *Appl. Phys. Lett.* **2002**, *80*, 1746–1748.

(4) Mullner, P.; Chernenko, V.; Kostorz, G. Stress-Induced Twin Rearrangement Resulting in Change of Magnetization in a Ni—Mn—Ga Ferromagnetic Martensite. *Scr. Mater.* **2003**, *49*, 129–133.

(5) Buehler, W. J.; Gilfrich, J.; Wiley, R. Effect of Low-Temperature Phase Changes on the Mechanical Properties of Alloys Near Composition TiNi. *J. Appl. Phys.* **1963**, *34*, 1475–1477.

(6) Ma, Y.; Zink, M.; Mayr, S. G. Biocompatibility of Single Crystalline Fe70Pd30 Ferromagnetic Shape Memory Films. *Appl. Phys. Lett.* **2010**, *96*, 213703.

(7) Allenstein, U.; Ma, Y.; Arabi-Hashemi, A.; Zink, M.; Mayr, S. Fe—Pd Based Ferromagnetic Shape Memory Actuators For Medical Applications: Biocompatibility, Effect of Surface Roughness and Protein Coatings. *Acta Biomater.* **2013**, *9*, 5845–5853.

(8) Zink, M.; Szillat, F.; Allenstein, U.; Mayr, S. G. Interaction of Ferromagnetic Shape Memory Alloys and RGD Peptides for Mechanical Coupling to Cells: from Ab Initio Calculations to Cell Studies. *Adv. Funct. Mater.* **2013**, *23*, 1383–1391.

(9) Chen, Q.; Wong, C.; Lu, W.; Cheung, K.; Leong, J.; Luk, K. Strengthening Mechanisms of Bone Bonding to Crystalline Hydroxyapatite in vivo. *Biomaterials* **2004**, *25*, 4243−4254.

(10) Sun, L.; Berndt, C. C.; Gross, K. A; Kucuk, A. Material Fundamentals and Clinical Performance of Plasma-Sprayed Hydroxyapatite Coatings: a Review. *J. Biomed. Mater. Res.* **2001**, *58*, 570−592.

(11) Klein, C. P.; de Blieck-Hogemrst, J.; Wolket, J.; De Groot, K. Studies of the Solubility of Different Calcium Phosphate Ceramic Particles in vitro. *Biomaterials* **1990**, *11*, 509−512.

(12) Narayanan, R.; Seshadri, S. K.; Kwon, T. Y.; Kim, K. H. Calcium Phosphate-Based Coatings on Titanium and its Alloys. *J. Biomed. Mater. Res., Part B* **2008**, *85*, 279−299.

(13) Xu, S.; Long, J.; Sim, L.; Diong, C. H.; Ostrikov, K. K. RF Plasma Sputtering Deposition of Hydroxyapatite Bioceramics: Synthesis, Performance, and Biocompatibility. *Plasma Processes Polym.* **2005**, *2*, 373−390.

(14) Kuhnemund, L.; Edler, T.; Kock, I.; Seibt, M.; Mayr, S. Epitaxial Growth and Stress Relaxation of Vapor-Deposited Fe−Pd Magnetic Shape Memory Films. *New J. Phys.* **2009**, *11*, 113054.

(15) Mahnke, G. J.; Seibt, M.; Mayr, S. Microstructure and Twinning in Epitaxial NiMnGa Films. *Phys. Rev. B: Condens. Matter Mater. Phys.* **2008**, *78*, 012101.

(16) Ma, Y.; Setzer, A.; Gerlach, J. W.; Frost, F.; Esquinazi, P.; Mayr, S. Freestanding Single Crystalline Fe− Pd Ferromagnetic Shape Memory Membranes−Role of Mechanical and Magnetic Constraints Across the Martensite Transition. *Adv. Funct. Mater.* **2012**, *22*, 2529−2534.

(17) Nelea, V.; Morosanu, C.; Iliescu, M.; Mihailescu, I. Microstructure and Mechanical Properties of Hydroxyapatite Thin Films Grown by RF Magnetron Sputtering. *Surf. Coat. Technol.* **2003**, *173*, 315−322.

(18) Giannozzi, P.; Baroni, S.; Bonini, N.; Calandra, M.; Car, R.; Cavazzoni, C.; Ceresoli, D.; Chiarotti, G. L.; Cococcioni, M.; Dabo, I.; Dal Corso, A.; de Gironcoli, S.; Fabris, S.; Fratesi, G.; Gebauer, R.; Gerstmann, U.; Gougoussis, C.; Kokalj, A.; Lazzeri, M.; Martin-Samos, L.; Marzari, N.; Mauri, F.; Mazzarello, R.; Paolini, S.; Pasquarello, A.; Paulatto, L.; Sbraccia, C.; Scandolo, S.; Sclauzero, G.; Seitsonen, A. P.; Smogunov, A.; Umari, P.; Wentzcovitch, R. M. Quantum Espresso: a Modular and Open-Source Software Project For Quantum Simulations of Materials. *J. Phys.: Condens. Matter* **2009**, *21*, 395502.

(19) We used the pseudopotentials Ni.pbe-nd-rrkjus.UPF, Mn.pbe-sp-van.UPF, Ga.pbe-nvan.UPF, Fe.pbe-nd-rrkjus.UPF, Pd.pbe-rrkjus.UPF, Ca.pbe-nsp-van.UPF, P.pbe-van_ak.UPF, O.pbevan_ak.UPF and H.pbe-van_ak.UPF from http://www.quantum-espresso.org.

(20) Jakob, A.; Muller, M.; Rauschenbach, B.; Mayr, S. Nanoscale Mechanical Surface Properties of Single Crystalline Martensitic Ni−Mn−Ga Ferromagnetic Shape Memory Alloys. *New J. Phys.* **2012**, *14*, 033029.

(21) Mayr, S. Energetic and Thermodynamic Aspects of Structural Transitions in Fe-Pd Ferromagnetic Shape Memory Thin Films: an ab initio Study. *Phys. Rev. B: Condens. Matter Mater. Phys.* **2012**, *85*, 014105.

(22) Monkhorst, H. J.; Pack, J. D. Special Points For Brillouin-Zone Integrations. *Phys. Rev. B* **1976**, *13*, 5188−5192.

(23) Methfessel, M.; Paxton, A. High-Precision Sampling for Brillouin-Zone Integration In Metals. *Phys. Rev. B: Condens. Matter Mater. Phys.* **1989**, *40*, 3616−3621.

(24) Bader, R. F. W. *Atoms in Molecules: A Quantum Theory*; Oxford University Press: Oxford, U.K., 1994.

(25) Kokalj, A. Computer Graphics and Graphical User Interfaces as Tools in Simulations of Matter at the Atomic Scale. *Comput. Mater. Sci.* **2003**, *28*, 155−168.

(26) BAM PowderCell 2.3. Available at http://www.bam.de/de/service/publikationen/powder_cell.htm.

(27) CaRIne Crystallography. Available at http://carine.crystallography.pagespro-orange.fr/.

(28) Martynov, V.; Kokorin, V. The Crystal Structure of Thermally- and Stress-Induced Martensites in Ni_2MnGa Single Crystals. *J. Phys. III* **1992**, *2*, 739−749.

(29) Hughes, J. M.; Cameron, M.; Crowley, K. D. Structural Variations in Natural F, OH, and Cl Apatites. *Am. Mineral.* **1989**, *74*, 870−876.

(30) Employing 0.40, 0.77, 1.05, 1.83, 1.42, 1.47, and 1.37 Å as covalent radii of H, O, P, Ca, Ni, Mn, and Ga, respectively.